Journal of Alloys and Compounds 509 (2011) 3705–3710

Contents lists available at ScienceDirect

Journal of Alloys and Compounds

journal homepage: www.elsevier.com/locate/jallcom

Phase evolution and dendrite growth in laser cladding of aluminium on zirconium

T.M. Yue[a,*], H. Xie[a], X. Lin[a], H.O. Yang[b]

[a] Advanced Manufacturing Technology Research Centre, Department of Industrial and Systems Engineering, Hong Kong Polytechnic University, Hung Hom, Kowloon, Hong Kong
[b] State Key Laboratory of Solidification Processing, Northwestern Polytechnical University, Xi'an 710072, PR China

ARTICLE INFO

Article history:
Received 28 May 2010
Accepted 23 December 2010
Available online 31 December 2010

Keywords:
Laser cladding
Aluminium
Zirconium
Phase evolution
Intermetallics
Dendrite growth

ABSTRACT

Aluminium was laser clad on a pure zirconium substrate using the blown powder method. The microstructure across the laser-clad coating was studied. Starting from the bottom to the top surface of the coating, a series of phase evolutions had occurred: $(Zr) \rightarrow (Zr) + AlZr_2 + AlZr_3 \rightarrow Al_4Zr_5 + Al_3Zr_2 \rightarrow Al_3Zr_2 + AlZr_2 \rightarrow Al_2Zr \rightarrow Al_2Zr + Al_3Zr$. This resulted in an epitaxial columnar crystal growth at the re-melt substrate boundary, a band of backward growth Al_3Zr_2 dendrites towards the lower half of the coating, and a two-phase eutectic dendritic growth of $Al_2Zr + Al_3Zr$ towards the top of the coating. The evolution of the various phases and microstructures is discussed in conjunction with the Al–Zr phase diagram, the criteria for planar interface instability, and the theory of eutectic growth under rapid solidification conditions (the TMK model).

1. Introduction

The results of previous research studies on the laser cladding of various metals on Mg-based substrates have shown that the technique is capable of improving the corrosion and wear resistance of magnesium alloys [1–4]. An essential factor for the success of laser cladding is the achievement of a strong metallurgical bond over the entire interface between the substrate and the clad-layer, with a limited amount of Mg going to the coating. The main challenges for achieving a high performance coating are to overcome the high chemical reactivity, the relatively low melting and boiling points of Mg-alloys, a high level of dilution of the coating, and ultimately to produce a defect-free coating with a strong metallurgically bonded interface. Previous studies have also shown that it is difficult to overcome the above problems and obtain good corrosion and wear properties by laser cladding of a single alloy composition on Mg alloys. Very often an interlayer, such as Al, needs to be laser deposited between the Mg substrate and the top protective coating in order to obtain a desirable coating [5]. In fact, in formulating the composition of the coating, properties such as the melting and vaporization temperatures, the solidification behaviour as well as the corrosion properties are important factors to be considered. The main reasons for choosing Al are that its melting point is only slightly higher than that of Mg and is lower than the vaporization point of Mg. This avoids excessive boiling of the Mg substrate and the creation of an extensive melt pool. Actually, aluminium is a commonly used alloying element for casting alloys of magnesium. As far as the cladding of aluminium on magnesium is concerned, previous work has shown that good interfacial bonding and good quality coatings can be produced [6,7]. Recently, Yue et al. [5] studied the solidification behaviour and phase evolution in the laser cladding of aluminium on magnesium substrates. However, the results of these studies also show that the problem of the high level of dilution cannot be easily overcome if only Al is used as the coating material.

In the course of the development of the cladding technique and the selection of suitable anti-corrosion coating alloys for Mg-based substrates, it was found that laser cladding of compositionally graded coatings on magnesium can bring further improvement in corrosion and wear resistance [4]. It is envisaged that cladding of a graded coating of Zr/Al on Mg substrates would result in significant improvement in corrosion resistance. Zr is chosen because it lies at the noble end of the galvanic series of metals in seawater. Moreover, it has excellent corrosion resistance in salt-laden environments [8]. This paper forms part of a wider study that investigates laser cladding of graded Zr/Al coatings on Mg substrates, and focuses on studying phase evolution in the rapid solidification of Al on Zr; while the study of the solidification behaviour and the evolution of the microstructure in laser cladding of aluminium on magnesium substrates has been reported previously [9].

---

* Corresponding author.
E-mail address: mftmyue@inet.polyu.edu.hk (T.M. Yue).

0925-8388/$ – see front matter © 2011 Elsevier B.V. All rights reserved.
doi:10.1016/j.jallcom.2010.12.173

Table 1
The laser processing parameters.

Laser power (kW)	Scanning velocity (mm/s)	Laser beam diameter (mm)	Powder feeding rate (g/min)
0.9	10	3	1.4

2. Experimental details

The laser cladding was carried out using a 4 kW continuous wave CO_2 laser from Prima North America Inc., which was equipped with a four-axis numerical control working table and a lateral powder feeder nozzle. In this study, the focal diameter of the laser beam was 3 mm, and the scanning rate was 10 mm/s. The experiment was conducted inside a controlled-atmosphere glove box, where high-purity argon gas was continuously supplied at a flow rate of 10 l per minute during the experiment to prevent the molten metal from oxidizing. The laser cladding experiment was conducted on a commercially pure zirconium (99.5 wt.%) substrate which had a surface area of 40 mm × 40 mm, and the coating powder was 99.9 wt.% pure Al with a mesh size of 200–300. Prior to the laser cladding experiment, the Al powder was dried in a vacuum oven for 24 h. In the experiment, the laser beam was directed onto the substrate to create a shallow molten pool, and the Al metal powder was delivered into the pool using a lateral powder feeder, with the aid of the flow from an argon gas jet. The feed angle between the substrate and the powder feeder nozzle was 60°. The metal powder was melted and subsequently re-solidified to form a laser-clad track. In order to create a coating, multi-tracks were produced with an overlapping percentage of 30%, and two layers were deposited. The total thickness of the coating was about 350 μm. A summary of the laser processing parameters is given in Table 1. The specimens for microscopic study were ground with a series of emery papers and then polished with 1 μm diamond abrasives. The microstructure of the material was revealed using a JEOL scanning electron microscope equipped with energy dispersive X-ray spectroscopy (EDX), and the specimens were in the unetched condition.

3. Results and discussion

3.1. Solidification of zone [I]

Fig. 1 shows the inter-relationship between the microstructure (Fig. 1a), the composition gradient across the coating (Fig. 1b), the Al–Zr binary equilibrium phase diagram (Fig. 1d), and the proposed solidification process during laser deposition of the second layer (Fig. 1c). The results of the EDX analysis (Fig. 1b) along the vertical direction of the coating show that with the deposition of Al, the concentration of Zr decreased to about 30 at.% towards the top surface of the coating [zone V]. Within such a compositional range, and according to the Al–Zr phase diagram, a series of reactions, eutectic, eutectoid, peritectic, and peritectiod, would have occurred. To investigate the phase evolution during laser deposition, the microstructure along the compositional gradient was studied using SEM. Figs. 2(a–f) show the backscattered SEM images of the microstructure of a cross section perpendicular to the coating. Figs. 2(b–f) correspond to the regions labelled [I]–[V] in Fig. 1a. The results of the EDX analysis of the phase composition at locations marked 1–7 are given in Table 2, which also presents the suggested phases based on the information of the Al–Zr phase diagram (Fig. 1d).

The microstructure close to the zirconium base is shown in Fig. 2(a), and reveals that a metallurgical bond was formed at the Zr/Al interface with no major solidification defects. An enlargement of the coating microstructure close to the re-melt boundary is shown in Fig. 2(b), which has a concentration of about 22 at.%Al. In this region, the microstructure comprises the phases of solid

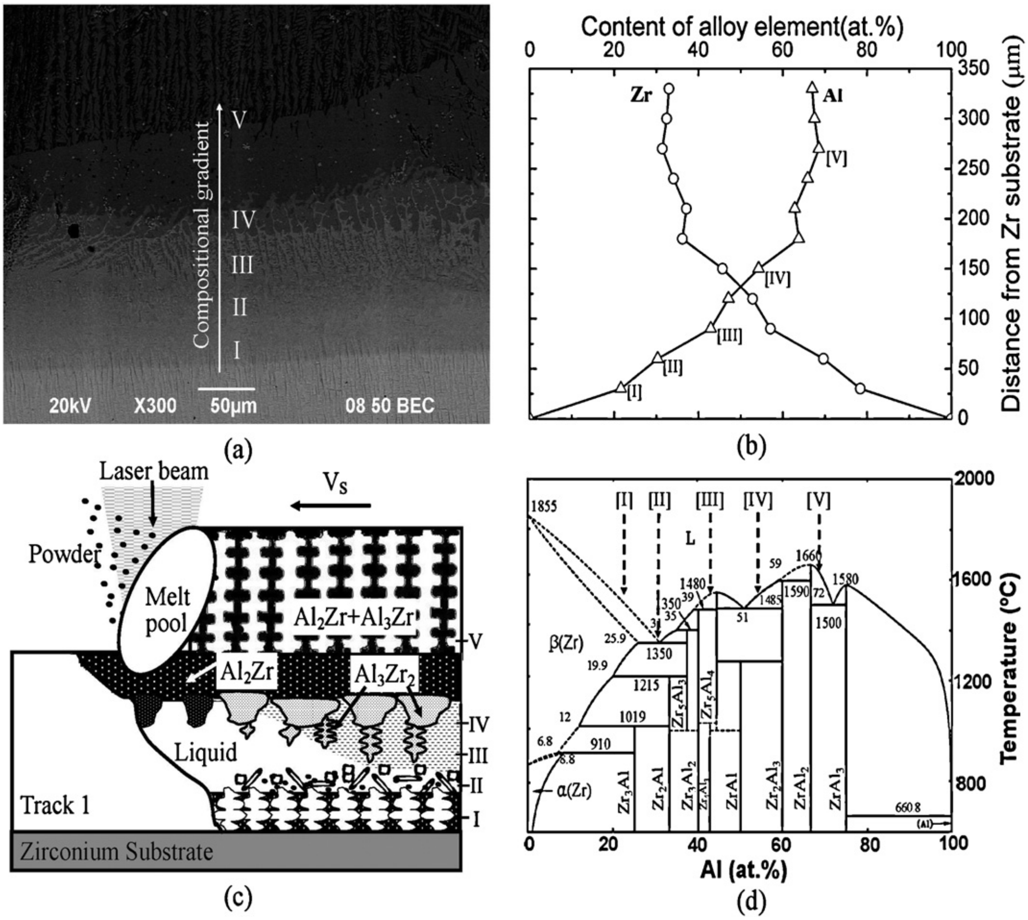

Fig. 1. Relationships between the composition profile, Al–Zr binary phase diagram and the corresponding microstructure in the laser-clad coating.

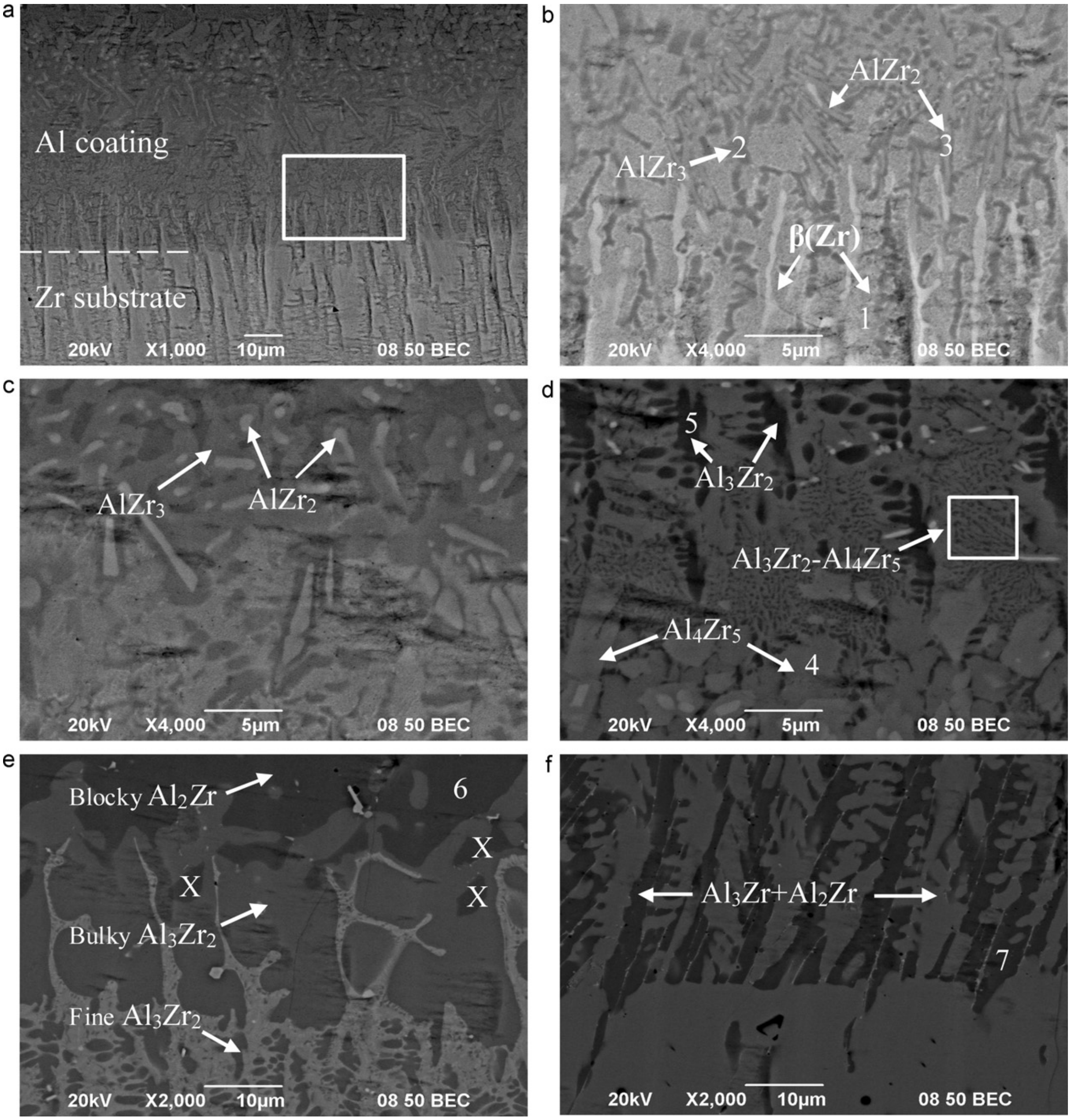

Fig. 2. Backscattered images of the Al–Zr coating showing the microstructure across the compositional gradient, (a) regions close to the re-melt substrate boundary, (b) an enlargement of (a), corresponding to zone [I] with 21.6 at.%Al, (c) corresponding to zone [II] with 30.4 at.%Al, (d) corresponding to zone [III] with 42.9 at.%Al, (e) corresponding to zone [IV] with 54.3 at.%Al, and (f) corresponding to zone [V] with 68.6 at.%Al.

solution β(Zr) in dendritic form, $AlZr_3$ and $AlZr_2$ intermetallics. The β(Zr) phase exhibits epitaxial columnar crystal growth. This is different from the planar growth that is often obtained at the re-melt boundary of a substrate in laser melting and cladding [10]. For directional solidification, the interface morphology will normally change from planar → cell → dendrite → cell → planar with increasing solidification velocity. In laser cladding and forming, the solidification velocity increases from zero at the bottom of the molten pool to a value close to the scanning velocity at the top; whereas, the temperature gradient is highest at the bottom of the molten pool and decreases towards the top of the molten pool. The bottom of the molten pool is where the solidification velocity has the lowest value, therefore a continuous planar growth normally occurs there. However, it has been demonstrated that under the conditions where the primary dendrite arm spacing is similar to the perturbation wavelength of instability of the planar growth, and if the growth orientation of the crystals in the melt pool is close to that of the underlying crystal, then epitaxial growth will prevail [10]. To examine the solidification condition in the present study of

Table 2
Summary of element analysis of phases marked as 1–7 in Fig. 2.

Location	Composition (at.%)		Phase
	Zr	Al	
1	78.55	21.45	β(Zr)
2	77.47	22.53	$AlZr_3$
3	67.68	32.32	$AlZr_2$
4	53.90	46.10	Al_4Zr_5
5	41.02	58.98	Al_3Zr_2
6	36.20	63.80	Al_2Zr
7	28.79	71.21	Al_3Zr

Table 3
Physical parameters used for the calculation of the predicted critical perturbation wavelength (λ_C), and the fastest growth perturbation wavelength (λ_F) as a function of the solidification velocity of primary β(Zr) phase.

Nominal composition (at.% Al)	21.6
Liquidus temperature (K)	1796.17
Gibbs–Thomson coefficient	3.68×10^{-7}
Equilibrium partition coefficient	0.595
Liquidus slope (K at.%$^{-1}$)	18.68
Thermal diffusivity (m^2 s^{-1})	9×10^{-9}
Activation energy for solute diffusion (J/mol)	4.7883×10^4
Prefactor of solute diffusion coefficient (m^2/s)	7.96×10^{-8}
Temperature gradient in solid and liquid (K/m)	10^6

whether epitaxial growth would occur, an analysis of planar interface stability based on the work of Trivedi and Kurz, was conducted [11]. In fact, they have extended the linear perturbation theory of Mullins and Sekerka [12] to the case of large thermal Peclet Numbers. According to Trivedi's analysis, the critical stability condition for a planar interface can be expressed as:

$$m_0 G_C \xi_C - \Gamma \omega^2 - (\bar{K}_S G_S \xi_S + \bar{K}_L G_L \xi_L) = 0 \tag{1}$$

where,

$$G_C = -\frac{(1-k_0) V C_0}{D_L} \tag{2}$$

$$\xi_L = \frac{\omega_L - V/a_L}{\bar{K}_S \omega_S + \bar{K}_L \omega_L} \tag{3}$$

$$\xi_S = \frac{\omega_S - V/a_S}{\bar{K}_S \omega_S + \bar{K}_L \omega_L} \tag{4}$$

$$\xi_C = \frac{\omega_C - V/D_L}{\{\omega_C - (V/D_L)(1-k_0)\}} \tag{5}$$

$$\bar{K}_S = \frac{K_S}{K_S + K_L}; \qquad \bar{K}_L = \frac{K_L}{K_S + K_L} \tag{6}$$

$$\begin{aligned} \omega_C &= \tfrac{V}{2D_L} + \left[\left(\tfrac{V}{2D_L}\right)^2 + \omega^2\right]^{1/2}; \\ \omega_L &= \frac{V}{2a_L} + \left[\left(\frac{V}{2a_L}\right)^2 + \omega^2\right]^{1/2}; \\ \omega_S &= -\frac{V}{2a_S} + \left[\left(\frac{V}{2a_S}\right)^2 + \omega^2\right]^{1/2} \end{aligned} \tag{7}$$

Whereas, $\omega = 2\pi/\lambda$ is the wave number, λ is the perturbation wavelength, k_0 and m_0 are the equilibrium partition coefficient and the liquidus slope, respectively. Γ is the Gibbs–Thomson coefficient, K_S and K_L are the thermal conductivities in the solid and liquid, respectively; while a_S and a_L are the thermal diffusivities in the solid and liquid, respectively. G_S and G_L are the temperature gradients in the solid and liquid at the unperturbed solid/liquid interface, respectively. D_L is the diffusion coefficient of solute in liquid, G_C is the solute concentration gradient in liquid at the unperturbed interface, and C_0 is the nominal concentration. Now, the critical perturbation wavelength for developing planar interface instability can be obtained by solving Eqs. (1)–(7).

Based on the above analysis, the predicted critical perturbation wavelength (λ_C), and the fastest growth perturbation wavelength (λ_F) were obtained (Fig. 3) as a function of the solidification velocity of the primary β(Zr) phase (22 at.%Zr), where the physical parameters used for the calculations are given in Table 3. The primary dendrite arm spacings of the Zr substrate and the β(Zr) phase adjoining the re-melt boundary were measured to be 7.1 μm and 6.7 μm, respectively; they are also included in Fig. 3. The results show that the measured primary arm spacing of the substrate, the measured dendrite spacing of the β(Zr) phase, and the wavelength of the initial fastest growth perturbation are very close to each other. This means that crystals at the re-melt boundary are favourable sites for the development of perturbations. On the other hand, the solute atoms that are rejected to the perturbation front will suppress the development of a continuous planar layer. As a result, perturbations will grow with a similar morphology as the underlying crystals, and continuing epitaxial dendrite growth of β(Zr) phase from the substrate was therefore obtained.

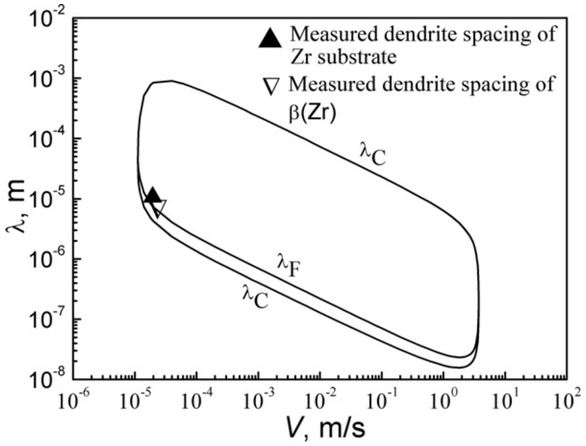

Fig. 3. The predicted critical perturbation wavelength (λ_C), and the perturbation wavelength with a maximum amplification rate (λ_F) as a function of the solidification velocity of primary β(Zr) phase at a cooling rate of 10^6 K/m. ▲ is the measured dendrite arm spacing of the Zr substrate and ▽ is the measured dendrite arm spacing of the β(Zr) phase.

3.2. Solidification of zones [II]–[IV]

At a further distance away from the Zr interface (zone II), the dendritic character of the Zr-rich solid solution phase becomes less apparent and its amount is reduced, while the amount of the $AlZr_3$ intermetallic compound is increased (Fig. 2c). The $AlZr_2$ phase is also commonly surrounded by the greyish black $AlZr_3$ phase. This can be explained by considering the Zr–Al phase diagram (Fig. 1d) at a composition of 30 at.%Al, where the relatively high Al content would decrease the stability of the primary β(Zr) phase and lead to the peritectiod reaction of $AlZr_2 + \beta(Zr) \rightarrow AlZr_3$. The encirclement of the $AlZr_2$ phase is believed to be due to non-equilibrium peritectoid transformation.

When the Al content reaches a level of 43 at.%Al (zone III), the microstructure mainly consists of Al_4Zr_5 and Al_3Zr_2 intermetallics (Fig. 2d). The Al_3Zr_2 phase grew in the form of directional dendrites, but it is interesting to note that its growth direction was opposite to the composition gradient and was towards the Zr substrate. Towards the end of the solidification in this zone, some fine Al_3Zr_2–Al_4Zr_5 eutectic structures were formed. As the Al concentration increased further along the compositional gradient, i.e. zone [IV], bulky Al_3Zr_2 dendrites were found, and lying above these dendrites a layer of blocky Al_2Zr intermetallic compound was found. It is believed that the blocky Al_2Zr zone was formed during laser cladding of the first Al layer. During laser cladding of the second Al layer, some relatively low melting point materials, including intermetallics, lying underneath this zone, were melted. This is highly possible because Al_2Zr has a high melting point of 1660 °C which is the highest among the Al–Zr intermetallics, according to phase diagram (Fig. 1d) [13]. Now, once a liquid phase is present around the Al_2Zr phase, a peritectic reaction $Al_2Zr + L \rightarrow Al_3Zr_2$ occurs, and thus leads to the formation of these bulky Al_3Zr_2 dendrites. However, due to non-equilibrium transformation, some small blocks of untransformed Al_2Zr (marked X in Fig. 2e) can been seen to have surrounded by the bulky Al_3Zr_2 phase. With a further decline in temperature upon cooling, the remaining liquid would enter into a hypereutectic region of the Al_4Zr_5–Al_3Zr_2 system (Fig. 1d), which means that Al_3Zr_2 crystals can nucleate directly on the surface of the peritectic product of bulky Al_3Zr_2 and form finer dendrites with a growth direction towards the Zr substrate (Figs. 2d and e). Finally, when the eutectic temperature is reached, the Al_4Zr_5–Al_3Zr_2 eutectic structure is formed (Fig. 2d).

3.3. Solidification of zones [V]

When the concentration of Al reaches a level of 69 at.%Al, that corresponds to the region of the Al_2Zr–Al_3Zr eutectic system in the Zr–Al phase diagram (Fig. 1 d), Al_2Zr dendrites and the $Al_2Zr + Al_3Zr$ eutectic should have formed upon solidification. However, the microstructure shown in Fig. 2f (zone V), reveals that a kind of epitaxial growth of two-phase dendrite of $Al_2Zr + Al_3Zr$ developed directionally in a vertical direction towards the top surface of the coating. This is considered to be due to the non-equilibrium effect of laser rapid solidification. To understand the eutectic growth behaviour of the Al_2Zr–Al_3Zr system, the growth condition was analysed using the TMK model [14], which predicts eutectic growth under rapid solidification conditions. Using the model, the eutectic interface temperature can be calculated by the relation,

$$T_e = T_{eut} + \Delta T_e \tag{8}$$

where T_{eut} is the nonequilibrium eutectic temperature, and ΔT_e is the nonequilibrium eutectic undercooling, which can be solved by the following two equations:

$$\lambda_e^2 V = \frac{a^L}{Q^L} \tag{9}$$

$$\lambda_e \Delta T_e = m a^L \left[1 + \frac{P}{P + \lambda(\partial P/\partial \lambda)}\right] \tag{10}$$

where λ_e is the lamellar spacing, and the definitions of the other terms are as follows:

$$a^L = 2\frac{\{(a_1^L/fm_1) + (a_2^L/((1-f)m_2))\}}{F(k_\upsilon)} \tag{11}$$

$$Q^L = \frac{1-k_\upsilon}{f(1-f)D_L}\left[P + \lambda\frac{\partial P}{\partial \lambda}\right] \tag{12}$$

$$m = \frac{m_1 m_2}{m_1 + m_2}F(k_\upsilon) \tag{13}$$

$$F(k_\upsilon) = 1 + \frac{k_0 - k(1 - \ln(k_\upsilon/k_0))}{1 - k_0} \tag{14}$$

$$k_\upsilon = \frac{k_0 + V/V_D}{1 + V/V_D} \tag{15}$$

$$P + \frac{\partial P}{\partial \lambda} = \sum_{n=1}^{\infty}\left(\frac{1}{n\pi}\right)^3 [\sin(n\pi f)]^2 \times \left[\frac{P_n}{\sqrt{1+p_n^2} - 1 + 2k_\upsilon}\right]^2 \frac{P_n}{\sqrt{1+p_n^2}} \tag{16}$$

$$P_n = \frac{2n\pi}{P_e} \tag{17}$$

where f is the volume fraction of the Al_2Zr phase associated with the $Al_2Zr + Al_3Zr$ eutectic, a_1^L and a_2^L are the capillarity constants of the Al_2Zr and Al_3Zr phases, P_e is the solutal Peclet Number for eutectic growth, m_1 and m_2 are the equilibrium liquidus slopes of Al_2Zr and Al_3Zr phases, respectively. $V_D = D_i/a_0$ is the interface diffusivity speed, with a_0 being the characteristic interface thickness and D_i the solute diffusivity across the interface. The physical parameters used for the calculations of the interfacial temperature and growth velocity are given in Table 4, and the results are presented in Fig. 4, in which, a maximum growth velocity of 14 mm/s with a sudden drop in eutectic interface temperature is predicted. The results suggest that beyond this maximum growth velocity, a cooperative lamellar structure cannot be obtained. According to the experimental conditions of this study, the laser scanning velocity was 10 mm/s, and is close to the predicted maximum growth velocity. Thus it is highly possible that in this study, the maximum growth velocity was exceeded and thus resulted in a two-phase dendrite growth instead of a cooperative lamellar structure.

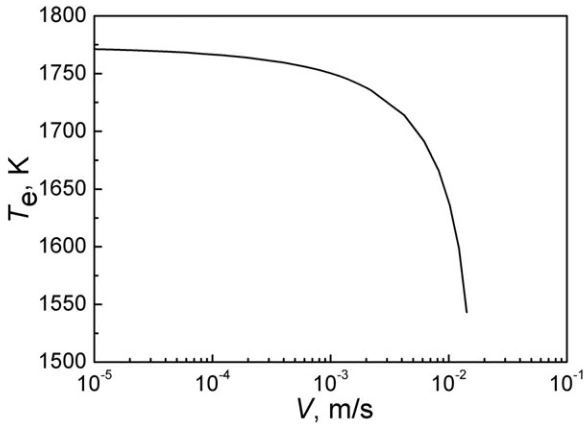

Fig. 4. Relationship between eutectic interface temperature (T_e) and growth velocity of the $Al_2Zr + Al_3Zr$ eutectic (V).

The dendrite arm spacing of the structure was also determined using the Hunt-Lu model [15,16]:

$$\lambda_d = \min\left\{24V'^{-1}, 5.0V'^{-b}\left(1 - \frac{G'}{V'}\right)^{0.5} G'^{-2(1-b)/3}\right\} \tag{18}$$

where

$$b = 0.3 + 1.9G'^{0.18} \tag{19}$$

$$G' = \frac{G\Gamma k}{\Delta T_0^2} \tag{20}$$

$$V' = \frac{V\Gamma k}{D\Delta T_0} \tag{21}$$

and ΔT_0 is the freezing range of the alloy. The physical parameters used for the calculation of the $Al_2Zr + Al_3Zr$ two-phase dendrite spacing are given in Table 4. The calculated spacing of the two-phase dendrite was 7.6 μm, which agrees reasonably well with the measured mean value of 10.4 μm.

Table 4
Physical parameters used for the calculation of interfacial temperature, growth velocity, and dendrite arm spacing of $Al_2Zr + Al_3Zr$.

Eutectic composition (at.% Al)	72
Eutectic temperature (K)	1773.15
Volume fraction of Al_2Zr phase	0.36
Length of eutectic line (at.% Al)	5.44
Equilibrium liquidus slope of Al_2Zr phase (K/at.%)	45.22
Equilibrium liquidus slope of Al_3Zr phase (K/at.%)	44.14
Capillarity constant of Al_2Zr phase (mK)	1.88×10^{-7}
Capillarity constant of Al_3Zr phase (mK)	3.35×10^{-7}
Prefactor of diffusion coefficient (m^2/s)	7.96×10^{-8}
Activation energy for solute diffusion (J/mol)	4.7883×10^{4}
Equilibrium partition coefficient of Al_2Zr phase	1×10^{-6}
Equilibrium partition coefficient of Al_3Zr phase	1×10^{-6}

4. Conclusions

An aluminium coating with a compositional gradient of up to 68.6 at.%Al was fabricated on a Zr substrate using laser cladding. A metallurgical bond with no major defect was formed on the Zr substrate. Within this wide composition range, a series of phase evolutions occurred, starting at the re-melt substrate boundary to the top of the coating: $(Zr) \rightarrow (Zr) + AlZr_2 + AlZr_3 \rightarrow Al_4Zr_5 + Al_3Zr_2 \rightarrow Al_3Zr_2 + AlZr_2 \rightarrow Al_2Zr \rightarrow Al_2Zr + Al_3Zr$. Two interesting phenomena have been noticed: backward dendritic growth of the Al_3Zr_2 phase occurred towards the lower half of the coating, and a two-phase $Al_2Zr + Al_3Zr$ eutectic dendritic structure towards the top coating. The former is believed to be due to the remelting of some relatively low melting point phases of the first deposited layer, and its formation mechanism can be explained in terms of the products of the peritectic reaction $Al_2Zr + L \rightarrow Al_3Zr_2$ and a direct crystal growth from the peritectic reaction product of Al_3Zr_2. As for the $Al_2Zr + Al_3Zr$ two-phase dendrite, its growth mechanism can be attributed to the condition that the experimental growth velocity was higher than the maximum growth velocity for a cooperative lamellar structure. The primary dendrite arm spacing of the two-phase $Al_2Zr + Al_3Zr$ eutectic structure was calculated using the Hunt-Lu model, and the result agrees reasonably well with the measured value.

Acknowledgements

The work described in this paper was fully supported by a grant from the Research Grants Council of the Hong Kong Special Administrative Region, China (Project No. PolyU 5345/08E). The authors would also like to thank the Hong Kong Polytechnic University and the Northwestern Polytechnical University for providing the research facilities.

References

[1] R. Galun, A. Weisheit, B.L. Mordike, J. Laser Appl. 8 (1996) 299–305.
[2] J.D. Majumdar, T. Maiwald, R. Galun, B.L. Mordike, Laser Eng. 12 (2002) 147–169.
[3] T.M. Yue, Y.P. Su, J. Mater. Sci. 42 (15) (2007) 6153–6160.
[4] T.M. Yue, T. Li, Surf. Coat. Technol. 202 (13) (2008) 3043–3049.
[5] T.M. Yue, T. Li, X. Lin, Metall. Mater. Trans. A 41 (1) (2010) 212–223.
[6] T.M. Yue, A.H. Wang, H.C. Man, Scripta Mater. 40 (1999) 303–311.
[7] S. Ignat, P. Sallamand, D. Grevey, M. Lambertin, Appl. Surf. Sci. 225 (2004) 124–134.
[8] R. Subramanian, S. Sircar, J. Mazumder, J. Mater. Sci. 26 (1991) 951–956.
[9] T.M. Yue, T. Li, Mater. Trans. 48 (5) (2007) 1064–1069.
[10] X. Lin, T.M. Yue, H.O. Yang, W.D. Huang, Mater. Sci. Eng. A391 (2005) 325–336.
[11] R. Trivedi, W. Kurz, Acta Metall. Mater. 34 (1986) 1663–1670.
[12] W. Mullins, R. Sekerka, J. Appl. Phys. 34 (1963) 323–329.
[13] H. Okamoto, J. Phase Equilib. 14 (1993) 259–260.
[14] R. Trivedi, P. Magnin, W. Kurz, Acta Metall. 35 (1987) 971–980.
[15] J.D. Hunt, S.Z. Lu, Metall. Mater. Trans. 27A (1996) 611–623.
[16] X. Wan, Q. Han, J.D. Hunt, Acta Mater. 45 (1997) 3975–3979.